

Exceptional thermoelectric properties in Na_2TlSb enabled by quasi-1D band structure

Øven A. Grimenes,^{1,*} Ole M. Løvvik,² and Kristian Berland^{1,†}

¹*Department of Mechanical Engineering and Technology Management,
Norwegian University of Life Sciences, NO-1432 Ås, Norway*

²*SINTEF Sustainable Energy Technology, Forskningsveien 1, NO-0314 Oslo, Norway*
(Dated: June 30, 2025)

Quasi-low-dimensional band structures in bulk high-symmetry materials can exhibit density of states (DOS) profiles akin to those of low-dimensional materials. A particular striking example is the full-Heusler compound Na_2TlSb , with valence band energy isosurfaces consisting of intersecting 2D-dimensional pockets forming a box-like structure, with the sides individually akin to the energy isosurfaces arising in one-dimensional (1D) quantum wells. The combination of high velocities (perpendicular to the pockets) and rapidly increasing DOS with energy (due to the low dimensionality) is extremely promising for thermoelectric applications. However, these beneficial properties could in principle be counteracted by high electronic scattering rates, and the benefits of for instance band convergence has been questioned precisely because of increased scattering rates. It is therefore critical to understand the electronic scattering nature of quasi-low-dimensional systems. In the current study, describing electronic transport properties of Na_2TlSb from first principles, we found that electronic scattering rates remained modest despite the high DOS. This was caused by the intricate interplay between several effects: (i) delocalized energetic isosurfaces giving rise to large momentum (\mathbf{q}) scattering paths with low wavefunction overlap, reducing the scattering probability; (ii) a high DOS resulting in a high free-carrier screening; (iii) a large portion of the scattering paths within the flat energy isosurfaces keeps the electron group velocity nearly constant, reducing the effective relaxation rates. The high velocity and modest relaxation time result in a high carrier mobility, which, together with the high DOS and beneficial DOS profile, results in excellent electron transport properties. Combined with an ultra-low lattice thermal conductivity of $\kappa_\ell < 1$ reported in literature, we predict a thermoelectric figure of merit ranging from 2.4 at 300 K to a maximum of 4.4 at 600 K. The n-type properties are also excellent, with a figure of merit from 1.5 at 300 K to 3.0 at 600 K.

I. INTRODUCTION

Thermoelectric (TE) materials are widely used in niche applications for cooling and electricity generation due to their high reliability, noiseless operation, and modular scalability [1]. However, their efficiency remains significantly lower than that of conventional vapor-liquid systems [1–3]. The efficiency of a TE material at a temperature T is linked to the TE figure of merit $zT = S^2\sigma T/(\kappa_e + \kappa_\ell)$, where S is the Seebeck coefficient and σ is the electrical conductivity, while κ_e and κ_ℓ are the electronic and lattice parts of the thermal conductivity. Most commercial TE materials have a zT no higher than 1. If values of 2 or higher could be realized, one would likely see a great increase in the application range [1, 4]. However, the properties involved in zT are highly interdependent, and increasing zT is non-trivial. Reducing κ_ℓ by e.g., nanostructuring [5], nanoinclusions [6], and isovalent alloying [7–9] has seen success across many systems, but can also have negative effects on the electronic transport properties. On the electronic side, a higher zT can be achieved by increasing the carrier mobility [10], by introducing nanostructures giving rise to energy filtering [11–13], or enhancing the electron density of states (DOS)

close to the band edge [14]. An increased DOS can be achieved by aligning bands or valleys through strain or alloying [15–18], by introducing resonant states [14, 19, 20].

Low-dimensional material structures, e.g., thin layers (2D materials) or nanowires (1D), can give rise to attractive density of state profiles and thus excellent electron transport properties [21, 22]. Such structures have seen some success for thermoelectric applications [23–25], but later analysis has revealed that the dimension of the nanostructures needs to be very small, as soon as multiple sub-bands contribute to the transport it counteracts the beneficial effects of low dimensionality. [26, 27]. Low-dimensional structures also pose significant challenges for low-cost fabrication. Encouragingly, conceptual studies indicate that band structures exhibiting 2D-like (tubes) and 1D-like (sheets) energy isosurfaces can arise even in bulk, isotropic materials [28–33]. This was also confirmed in our recent study of the TE properties of CsK_2Sb , which hosted extended tube-like energetic isosurfaces close to the Fermi level that could be enhanced by strain [33]. Another example, PbTe [34], host extended sheet-like energetic isosurfaces in the valence band. As do the related full-Heusler compounds Li_2TlBi and Li_2InBi , [35] but in these cases they are located too far below the valence band maximum (VBM) to considerably contribute to the electron transport.

A system with extended energy isosurfaces close to the VBM is the full-Heusler Na_2TlSb (see Fig. 1). This material has previously been studied by Yue *et al.* [36], pre-

* oven.andreas.grimenes@nmbu.no

† kristian.berland@nmbu.no

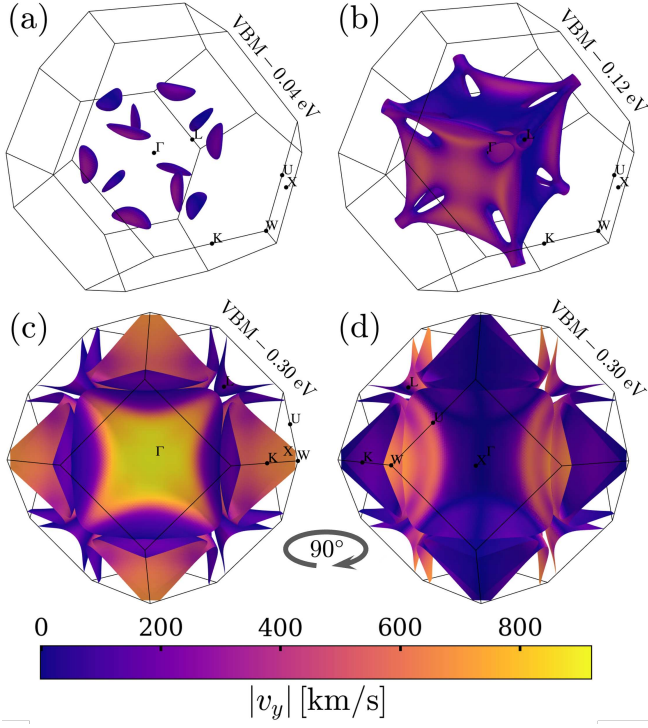


FIG. 1. Energy isosurfaces of the Na_2TlSb valence band obtained with density functional theory. Initially (a), the valence band forms 12 Fermi pockets between Γ and K , but these merge into continuous box-like isosurfaces shown at 0.12 eV below the VBM in (b). The box surfaces consist of pairs of sheets giving a hollow Fermi surface. Moving to 0.30 eV below the VBM, the isosurface expands to six overlapping sheets, shown from two different perspectives in (c) and (d). The color gradient indicates the y -component of the electron group velocity, highlighting how the sheets contribute individually to transport in the direction perpendicular to the sheets.

dicting it to have an exceptionally high zT , but this study emphasized the origin of the ultralow κ_ℓ and not electronic properties. The system itself was independently identified as a very low κ_ℓ material by us [37]. In the current study, we investigate the TE potential of Na_2TlSb with a focus on the interplay between the electronic band structure and the electronic scattering. Understanding the role of scattering is critical for the assessment of TE properties, because the high DOS associated with low-dimensional band structures also gives rise to many scattering channels that could limit electronic mobility.

II. THEORY

A. Electron transport

Electron transport properties were modeled with the Boltzmann transport equation in the relaxation time approximation [38–40]. In this theory, the electron trans-

port properties can be expressed with the generalized transport coefficients

$$\mathcal{L}^{(\alpha)} = q^2 \int_{-\infty}^{\infty} d\varepsilon \Sigma(\varepsilon) W^{(\alpha)}(\varepsilon), \quad (1)$$

where q is the elementary charge, $W^{(\alpha)}$ are Fermi selection functions,

$$W^{(\alpha)}(\varepsilon) = (\varepsilon - \varepsilon_F)^\alpha \left(\frac{\partial f}{\partial \varepsilon} \right), \quad (2)$$

where ε_F is the Fermi level and f is the Fermi-Dirac distribution function, and the transport distribution function is given by

$$\Sigma(\varepsilon) = \sum_n \int_{\text{BZ}} \frac{d\mathbf{k}}{8\pi^3} \tau_{n\mathbf{k}} v_{n\mathbf{k}} \otimes v_{n\mathbf{k}} \delta(\varepsilon - \varepsilon_{n\mathbf{k}}), \quad (3)$$

where $v_{n\mathbf{k}}$ and $\tau_{n\mathbf{k}}$ are the group velocity and relaxation time of a state with index $n\mathbf{k}$.

In terms of the transport coefficients, the TE properties σ , S , and κ_e can, at the temperature T , be expressed as

$$\sigma = \mathcal{L}^{(0)}, \quad (4)$$

$$S = \frac{\mathcal{L}^{(1)}}{qT\mathcal{L}^{(0)}}, \quad (5)$$

$$\kappa_e = \frac{1}{q^2 T} \left[\mathcal{L}^{(2)} - \frac{(\mathcal{L}^{(1)})^2}{\mathcal{L}^{(0)}} \right]. \quad (6)$$

B. Electron scattering

Elastic relaxation rates were computed in the momentum relaxation time approximation (MRTA) [40–42]. The transition rate between two states is given by

$$\Gamma_{n\mathbf{k} \rightarrow m\mathbf{k}+\mathbf{q}} = \frac{2\pi}{\hbar} |g_{nm}(\mathbf{k}, \mathbf{q})|^2 \delta(\varepsilon_{n\mathbf{k}} - \varepsilon_{m\mathbf{k}+\mathbf{q}}), \quad (7)$$

where $g_{nm}(\mathbf{k}, \mathbf{q})$ are effective coupling matrix elements. The corresponding effective relaxation rate of a state is given by

$$\Gamma_{n\mathbf{k}}^{\text{MRTA}} = \sum_m \int \frac{d\mathbf{q}}{\Omega_{\text{BZ}}} \Lambda_{nm}(\mathbf{k}, \mathbf{q}) \Gamma_{n\mathbf{k} \rightarrow m\mathbf{k}+\mathbf{q}}, \quad (8)$$

where Ω_{BZ} is the Brillouin-zone volume. The geometric factor

$$\Lambda_{nm}(\mathbf{k}, \mathbf{q}) = \left[1 - \frac{\mathbf{v}_{n\mathbf{k}} \cdot \mathbf{v}_{m\mathbf{k}+\mathbf{q}}}{|\mathbf{v}_{n\mathbf{k}}|^2} \right] \quad (9)$$

quantifies the relative importance of forward- and back-scattering on the effective transport properties.

For inelastic scattering, the MRTA does not hold [40, 42], and scattering rates were computed using the self-energy relaxation time approximation (SERTA) [40, 42],

i.e., the integral is performed without the factor. For polar-optical phonons, transition rates are given by

$$\Gamma_{n\mathbf{k} \rightarrow m\mathbf{k}+\mathbf{q}} = \frac{2\pi}{\hbar} |g_{nm}(\mathbf{k}, \mathbf{q})|^2 \quad (10)$$

$$\times [(n_{\mathbf{q}} + 1 - f_{m\mathbf{k}+\mathbf{q}})\delta(\varepsilon_{n\mathbf{k}} - \varepsilon_{m\mathbf{k}+\mathbf{q}} - \hbar\omega_{\mathbf{q}}) + (n_{\mathbf{q}} + f_{m\mathbf{k}+\mathbf{q}})\delta(\varepsilon_{n\mathbf{k}} - \varepsilon_{m\mathbf{k}+\mathbf{q}} + \hbar\omega_{\mathbf{q}})],$$

where $n_{\mathbf{q}}$ and $\omega_{\mathbf{q}}$ are the Bose-Einstein occupancy and frequency of the optical phonon with wave vector \mathbf{q} , respectively. The corresponding relaxation rates are given by

$$\Gamma_{n\mathbf{k}}^{\text{SERTA}} = \sum_m \int \frac{d\mathbf{q}}{\Omega_{\text{BZ}}} \Gamma_{n\mathbf{k} \rightarrow m\mathbf{k}+\mathbf{q}}. \quad (11)$$

Within AMSET [40], which was used in this study, the coupling terms involved in the scattering mechanisms are approximated as a product of a perturbing potential and the wavefunction overlap between the initial and final state,

$$M_{mn}(\mathbf{k}, \mathbf{q}) = \langle m\mathbf{k} + \mathbf{q} | e^{i\mathbf{q} \cdot \mathbf{r}} | n\mathbf{k} \rangle. \quad (12)$$

Both M and the perturbing potential depend on the momentum transfer \mathbf{q} . The perturbative potential is given in terms of effective coupling elements for the acoustic deformation potential (ADP), ionized impurity (IMP), and polar optical phonon (POP) scattering, which can be expressed as

$$g_{nm}^{\text{ADP}}(\mathbf{k}, \mathbf{q}) = A^{\text{ADP}} M_{mn}(\mathbf{k}, \mathbf{q}), \quad (13)$$

$$g_{nm}^{\text{POP}}(\mathbf{k}, \mathbf{q}) = A^{\text{POP}} \frac{M_{mn}(\mathbf{k}, \mathbf{q})}{\sqrt{\mathbf{q}^2 + \beta_{\infty}^2}}, \quad (14)$$

$$g_{nm}^{\text{IMP}}(\mathbf{k}, \mathbf{q}) = A^{\text{IMP}} \frac{M_{mn}(\mathbf{k}, \mathbf{q})}{\mathbf{q}^2 + \beta_s^2}, \quad (15)$$

where the prefactors A are independent of the amplitude of q . The high-frequency inverse free-carrier screening length is given by

$$\beta_{\infty}^2 = \frac{e^2}{\epsilon_{\infty} k_{\text{B}} T} \int \frac{d\varepsilon}{V} \text{DOS}(\varepsilon) f(\varepsilon) (1 - f(\varepsilon)), \quad (16)$$

while the static inverse free-carrier screening length β_0 is calculated the same way, but uses the static dielectric constant ϵ_s in place of the high-frequency ϵ_{∞} .

The prefactor in the perturbing potential of ADP scattering is given by

$$A^{\text{ADP}} = \sqrt{k_{\text{B}} T} \sum_{i=l, t_1, t_2} \frac{\tilde{\mathbf{D}}_{n\mathbf{k}} : \hat{\mathbf{S}}_i}{c_i \sqrt{\rho}}, \quad (17)$$

where $\tilde{\mathbf{D}}_{n\mathbf{k}}$ is the velocity-corrected deformation potential $\mathbf{D}_{n\mathbf{k}} + v_{n\mathbf{k}} \otimes v_{n\mathbf{k}}$. Here $:$ denotes the double inner product, $\hat{\mathbf{S}}$ is unit strain, c is the sound velocity, and ρ is the mass density. The sum runs over the longitudinal l and the two transverse t_1, t_2 directions for $\hat{\mathbf{S}}$ and c .

For IMP, the prefactor is given by

$$A^{\text{IMP}} = \frac{n_{ii}^{1/2} Z e}{\hat{\mathbf{n}} \cdot \epsilon_s \cdot \hat{\mathbf{n}}}, \quad (18)$$

where $n_{ii} = (n_h - n_e)/Z$ is the concentration of ionized impurities, Z is the impurity charge state, and $\hat{\mathbf{n}}$ is a unit vector in the direction of scattering,

For POP scattering,

$$A^{\text{POP}} = \left[\frac{\hbar\omega_{\text{po}}}{2} \right]^{1/2} \left(\frac{1}{\hat{\mathbf{n}} \cdot \epsilon_{\infty} \cdot \hat{\mathbf{n}}} - \frac{1}{\hat{\mathbf{n}} \cdot \epsilon_s \cdot \hat{\mathbf{n}}} \right)^{1/2}. \quad (19)$$

Here, ω_{po} is an effective weighted optical phonon frequency given by $\omega_{\text{po}} = \sum_{\nu} \omega_{\Gamma\nu} w_{\nu} / \sum_{\nu} w_{\nu}$, where $\omega_{\Gamma\nu}$ is the phonon frequency of branch ν at Γ and $w_{\nu} = \sum_{\gamma} [m_{\gamma} \omega_{\mathbf{q}\nu}]^{-1/2} \times [\mathbf{q} \cdot \mathbf{Z}_{\gamma}^* \cdot \mathbf{e}_{\gamma\nu}]$, where m is the atomic mass of atom γ , \mathbf{Z}_{γ}^* is the Born effective charge, and $\mathbf{e}_{\gamma\nu}$ is a phonon eigenvector.

The total (TOT) scattering rate was obtained as the sum of the different considered scattering mechanisms according to Matthiessen's rule [43]:

$$\Gamma_{n\mathbf{k}}^{\text{TOT}} = \Gamma_{n\mathbf{k}}^{\text{ADP}} + \Gamma_{n\mathbf{k}}^{\text{IMP}} + \Gamma_{n\mathbf{k}}^{\text{POP}}. \quad (20)$$

C. Computational details

All transport properties were computed using AMSET [40] version 0.5.0. Input electronic band structure and physical properties were calculated using density functional theory (DFT) as implemented in the Vienna Ab initio Simulation Package (VASP) [44, 45]. The vdW-DF-cx [46–48] exchange correlation functional was used to relax the crystal structure, calculate elastic constants using finite differences [49], and the ionic contribution to the dielectric constant and phonon frequencies by density functional perturbation theory (DFPT) [50]. As vdW-DF-cx only accounts for exchange at the generalized-gradient approximation level, band gaps can be underestimated. Therefore, the hybrid functional HSE06 [51] was used to calculate the high-frequency dielectric constant, deformation potentials, and the electronic band structure used for transport calculations. A plane-wave cutoff of 520 eV (identical to that used by the Materials Project (MP) [52]) was used and the number of electrons in the basis set was 7 (Na), 13 (Tl), and 5 (Sb). All DFT calculations included spin-orbit coupling (SOC). The initial crystal structure was retrieved from the MP database (mp-866132) and relaxed to within 5.0×10^{-5} eV/Å. A second relaxation was subsequently performed to avoid errors related to Pulay stress. Relaxations, DFPT, finite differences for elastic constants, and deformation potentials were calculated using a $12 \times 12 \times 12$ \mathbf{k} -point grid. The final band structure for transport used a $24 \times 24 \times 24$ \mathbf{k} -point grid. In the transport calculations, the band structure was interpolated to a $63 \times 63 \times 63$ \mathbf{k} -point grid. The high-frequency dielectric constant ϵ_{∞} was calculated at

the HSE06 level, computing the momentum matrix elements and the electronic levels using a $24 \times 24 \times 24$ k-point grid using 80 bands at the independent particle level. We used an in-house code for computing ϵ_∞ from longitudinal matrix elements extracted from VASP. This choice was made since ϵ_∞ was found to be highly dependent on the band gap, and we found it to require careful convergence with the number of \mathbf{k} -points, but quite insensitive to whether local field corrections were included, and hence neglected.

For computing zT , κ_ℓ was taken from Ref. [36] and interpolated using splines, listed in App. A.

III. RESULTS

A. Materials properties

Table I lists the lattice constant, elastic constants C_{ij} , static ϵ_s and high-frequency dielectric constant ϵ_∞ obtained for Na_2TlSb . The lattice constant of 7.53 \AA is slightly higher than the value of 7.49 \AA reported by Yue *et al.*, using PBEsol [53]. The low C_{ij} values result in a low velocity of sound, c , in Eq. 17. The low c can also partly explain the low κ_ℓ [54]. Low elastic constants can also give rise to high electron scattering rates, as they can increase the ionic polarizability (i.e., giving a large A^{POP}), and hence increase the POP scattering.

TABLE I. The lattice constant, elastic constants, dielectric tensors, and average optical phonon frequency of Na_2TlSb .

a [\AA]	7.53
C_{11} [GPa]	46.3
C_{12} [GPa]	16.8
C_{44} [GPa]	24.9
ϵ_s	115.6
ϵ_∞	30.3
ω_{po} [THz]	1.55

B. Electronic structure

Figure 2 shows the electronic band structure and density of states (DOS) corresponding to the energy isosurfaces of Fig. 1, of which the band topology closely resembles those of an ideal 1D material [32]. The low-dimensional band structure can explain the rapidly rising valence-band DOS, as compared to the conduction-band DOS. Both the conduction and valence bands are strongly dominated by p-orbital character, mostly associated with Sb for the valence band and Tl for the conduction band. The band character is akin to PbTe and analogous compounds such as Li_2TlBi [34, 35], where Tl (Sb) takes the role of Pb (Te), with Na as a spectating cation.

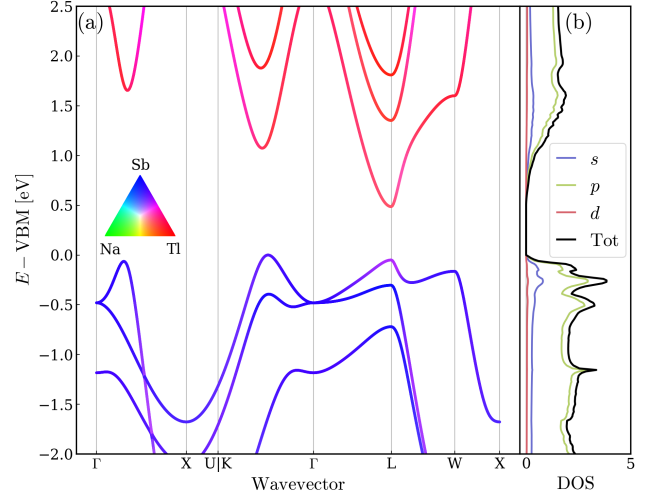


FIG. 2. (a) Atom-projected electronic band structure and (b) the orbital and total electronic DOS of Na_2TlSb calculated with the HSE06 functional and spin-orbit coupling.

C. Electronic transport

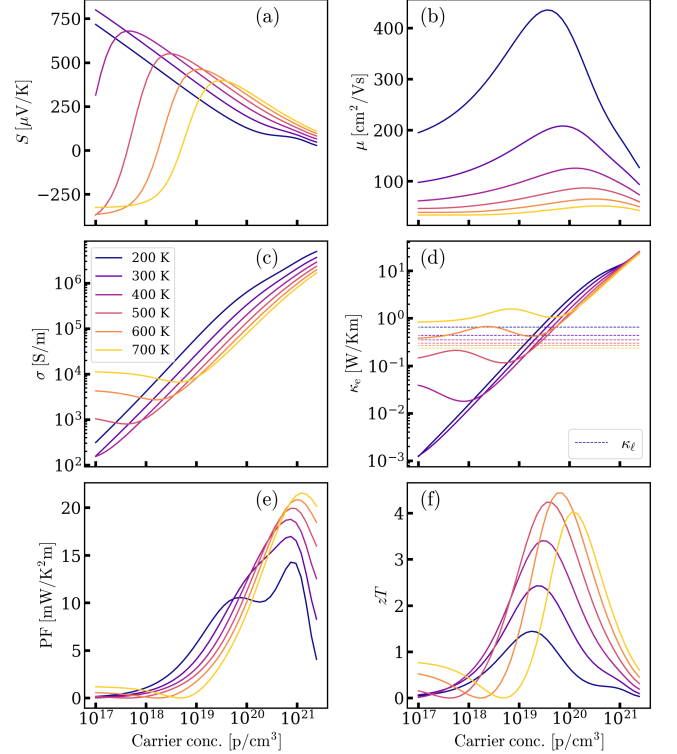


FIG. 3. The Seebeck coefficient (S), mobility (μ), electrical conductivity (σ), electron thermal conductivity (κ_e), power factor (PF), and figure of merit (zT) of p-type Na_2TlSb at temperatures 200–700 K.

Figure 3 shows thermoelectric transport properties at

different temperatures as a function of p-carrier concentration. With zT surpassing a value of 4.4 at 600 K, we confirm earlier identification of Na_2TlSb as an extremely promising thermoelectric material [36]. The combination of high S and σ yields a maximum high power factor of more than $15 \text{ mW/K}^2\text{m}$ for most temperatures. Combined with the ultra-low κ_ℓ , this gives a promising material at high temperatures, but it also reaches an exceptional optimal p-type zT of 2.4 at room temperature (300 K). The fact that zT remains high across such a wide temperature span can also be understood from the high low-temperature mobility μ . The mobility decreases markedly with temperature, which can be understood from increasing electron-phonon scattering due to the sharply increasing DOS, as discussed in Sec. III D. A key factor limiting zT is the electronic thermal conductivity κ_e is often larger in magnitude than κ_ℓ , reaching as high as 0.85 W/mK at optimal doping concentration. An interesting aspect of the large asymmetry between the valence and conduction DOS, is that charge neutrality biases μ_F towards the conduction band, and quite large p-doping is needed to overcome bipolar transport. This is seen at 700 K, where S changes sign around $5 \times 10^{19} \text{ h/cm}^3$ (a). Similarly, both σ and κ_e flatten out at low carrier concentrations as the conduction band begins to contribute to transport.

Fig. 4 displays (a) the p-type and (b) n-type zT as a function of temperature over the range 200–700 K. Each is plotted for different carrier concentrations around the optimal one for zT (N_{opt}). A consequence of the high zT at a wide range of temperatures is that the temperature-averaged zT can also be very high. This is shown by the dashed lines, which indicate the maximal temperature-averaged zT (zT_{avg}) from 300 to 700 K, using a fixed doping concentration of $5.7 \times 10^{19} \text{ h/cm}^3$ and $4.3 \times 10^{18} \text{ e/cm}^3$ for p- and n-type doping, respectively. Even higher values would be obtained with graded doping in the TE legs. The high n-type zT , which arises from fast electrons around the L-valley, also highlights the promise of Na_2TlSb for single-material thermoelectric devices.

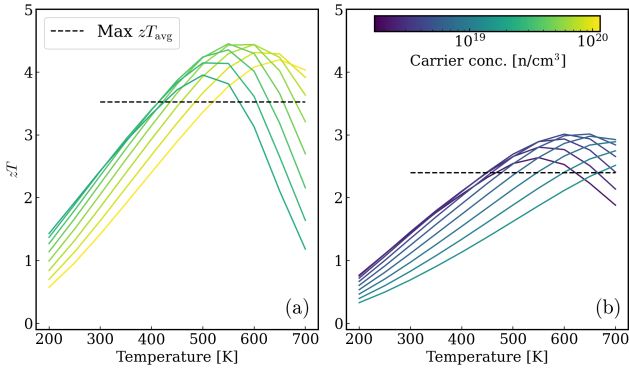


FIG. 4. zT as a function of temperature for various carrier concentrations for (a) p- and (b) n-type. The highest achievable average zT over the range 300–700 K is also indicated.

D. Electronic scattering rates

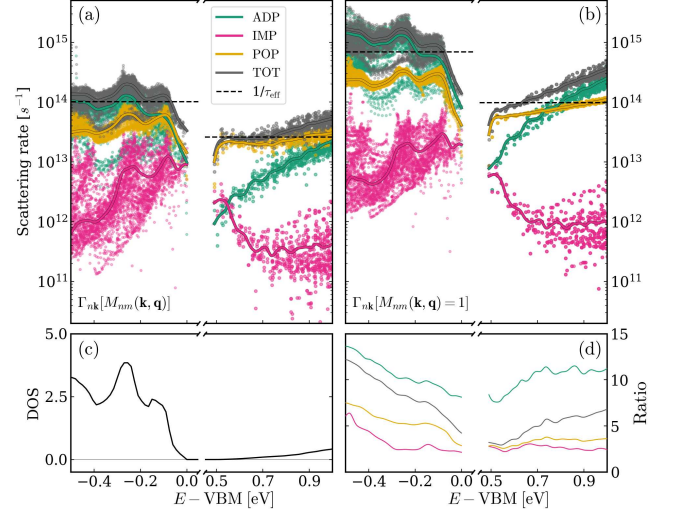


FIG. 5. Scattering rates of the valence and conduction bands of Na_2TlSb based on ADP, IMP, and POP scattering, as well as the total scattering rate (TOT) at 600 K. The solid lines show a Gaussian-smeared average of each scattering mechanism. In (a), the effect of wavefunction overlaps is included, while in (b), the overlap is set to unity for all transition rates. The electronic DOS is shown in (c). In (d), the ratio between the running average scattering with (from a) and without (from b) the effect of wavefunction overlap is displayed.

Figure 5 (a) displays the scattering rates $\Gamma_{n\mathbf{k}}$ at 600 K with respect to the charge carrier energy for the respective n- and p-type N_{opt} at this temperature. The wide range of scattering rates reflects a significant \mathbf{k} -dependence in relaxation times. For clarity, running averages (Gaussian smeared) are also shown, highlighting their energy dependence. As expected from the vastly larger DOS, p-type scattering is larger than n-type. This can be seen by the dashed lines which indicate $1/\tau_{\text{eff}}$, which is the effective constant scattering rate that results in the same mobility as that obtained with full scattering [33]. Interestingly, despite the huge DOS, shown in (c), the effective relaxation time of the p-doped material at 600 K is quite similar to the standard CRTA choice of 10 fs. For both p- and n-type, POP is the strongest scattering mechanism close to the band gap. For p-type, ADP becomes dominant further away from the band gap. This is not the case for n-type, however, where ADP scattering is much smaller. Similarly, IMP scattering is larger for p-type compared to n-type, but it is still not a major contribution to the total scattering rate for either.

ADP scattering rates for different energies reflects the magnitude of the DOS, shown in 5 (c), and are far larger for p-type than n-type (deformation potentials are comparable, see Ref. [56]). This trend can be understood from the lack of an explicit \mathbf{q} -dependence for ADP scattering (see 13), allowing for potentially large scattering rates across of the Brillouin zone. However, \mathbf{q} -

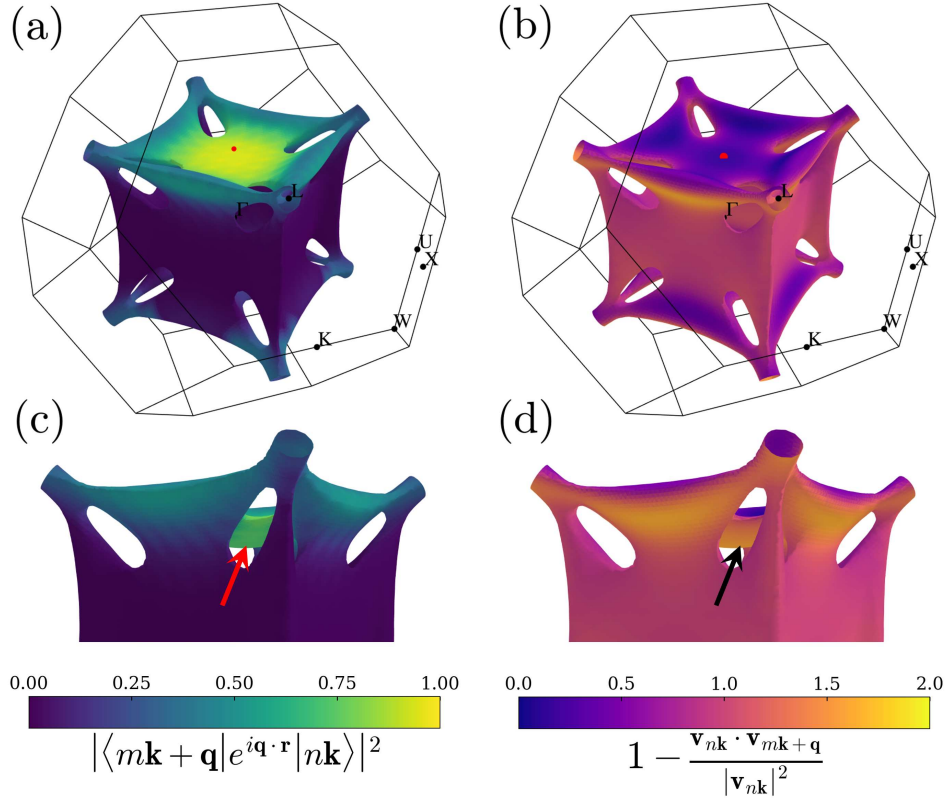


FIG. 6. Energy isosurfaces of the Na₂TlSb valence band at 0.12 eV below the VBM. (a) Colored by the wavefunction overlap between initial and final state $|M_{mn}(\mathbf{k}, \mathbf{q})|^2 = \langle m\mathbf{k} + \mathbf{q} | e^{i\mathbf{q} \cdot \mathbf{r}} | n\mathbf{k} \rangle|^2$ (Eq. 12), from a selected initial \mathbf{k} -point marked with a red dot on the isosurface. (b) Similarly colored by the geometric MRTA factor $\Lambda_{nm}(\mathbf{k}, \mathbf{q})$, see Eq. 9. Panels (c) and (d) show the same surfaces from a different perspective. The surfaces are plotted with IFermi [55].

dependence do enter through the wavefunction overlap $M_{mn}(\mathbf{k}, \mathbf{q}) = \langle m\mathbf{k} + \mathbf{q} | e^{i\mathbf{q} \cdot \mathbf{r}} | n\mathbf{k} \rangle$ and the MRTA factor Λ , as shown in Fig. 6. Panel (a) and (c) shows the wavefunction overlaps remain quite large on the upper side of the box-like isosurface, but the overlap with the other sides is nearly zero. The low overlap can be understood from the dominant p-character of the valence band (Fig. 2), i.e., wavefunctions on different sides are (approximately) orthogonal. Fixing the overlap to $M = 1$ increases the scattering rates by a factor of 7 for p-type and 4 for n-type, as illustrated by comparing panel (a) and (b) in Fig. 5, of the relative factor (d). They also show that the effects of setting $M = 1$ is far largest for ADP-scattering with its lack of an explicit \mathbf{q} -dependence, but is also very significant for the other scattering mechanisms. Due to ADP being a larger relative contribution to p-type, M also has a larger effect on the total scattering rate for p-type.

The geometric MRTA factor $\Lambda_{nm}(\mathbf{k}, \mathbf{q}) = 1 - \mathbf{v}_{n\mathbf{k}} \cdot \mathbf{v}_{m\mathbf{k} + \mathbf{q}} / |\mathbf{v}_{n\mathbf{k}}|^2$ (Eq. 9) for elastic scattering is shown in Fig. 6 (b/d). This factor has values around 0 for forward scattering, 1 for perpendicular scattering, and 2 for backwards scattering. The box-like geometry of the Na₂TlSb energetic isosurface makes this geometric factor very evident. It is very low for same-side scattering, where M is

largest, and has higher values to the other faces, where M is low. However, to the inside of the box is has both a large M and Λ , resulting in strong scattering.

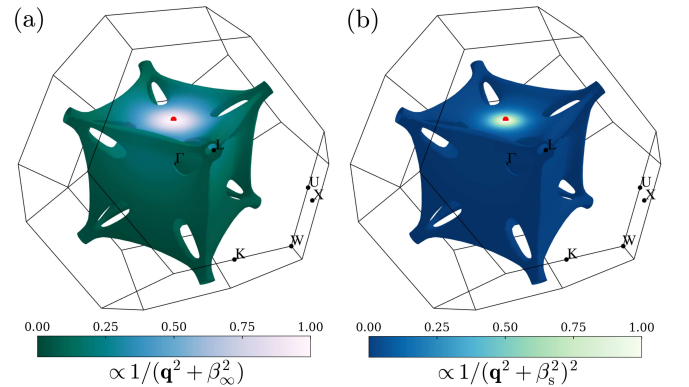


FIG. 7. Energy isosurfaces of the Na₂TlSb valence band at 0.12 eV below VBM. (a) Colored by the normalized \mathbf{q} -dependence $1/(\mathbf{q}^2 + \beta_\infty^2)$ for POP scattering and (b) the normalized \mathbf{q} -dependence $1/(\mathbf{q}^2 + \beta_s^2)^2$ for IMP scattering from a sample \mathbf{k} -point.

Fig. 7 shows the contributions of the explicit \mathbf{q} -dependent factors in POP (a, Eq. 14) and IMP (b, Eq. 15)

scattering. It underlines how these scattering mechanisms are strongly localized in \mathbf{k} -space, and can in part explain why POP scattering rates have similar n-type and p-type magnitudes despite much large energy isosurfaces on the p-side. The increased scattering due to larger energy isosurfaces is also counteracted by increased screening (Eq. 14) at optimal carrier concentrations N_{opt} , which is much higher when the DOS is large. The β_{∞}^2 of p-type is 17 times higher than that of n-type for their respective N_{opt} . The effect of POP scattering is given in Ref. [56]. Interestingly, without free-carrier screening the p-type zT_{avg} is only marginally reduced since the increased scattering reduces bipolar transport at higher temperatures, see zT values in Ref. [56]. While IMP scattering is even more local, it is still stronger between the outer and inner part of the energy isosurface than for the n-type Fermi pockets where distances quickly increase above the conduction band minimum. The high N_{opt} for p-type also make the prefactor (eq. 18) larger. Even if POP and IMP scattering are short-ranged, they can be very strong, particularly close to the band edges (Fig. 5) due to large scattering prefactors and divergent $1/q$ behavior in the small \mathbf{q} limit.

IV. DISCUSSION

A concern in materials with high DOS is that excessive electron scattering can cripple the electron mobility, in line with the numerous tradeoffs limiting the development of high-performing TE materials [57]. However, in the AMSET-based analysis of this paper, we have found this is not the case for Na_2TiSb , an extreme example of extended 2D-like energy isosurfaces akin to those of 1D-like nanostructured materials. Several compounding effects contribute to counteract the effect of the high DOS, explaining why this material is predicted to have such a high zT , including the role of momentum-dependence of dominant scattering rates, the parity of wavefunction, and charge-carrier screening at optimal carrier concentrations. However, it is critical to remark that other mechanisms not accounted for here could increase the scattering rates. Electron-electron scattering, which is usually insignificant for lightly doped semiconductors, could be noteworthy at carrier concentrations around p-type N_{opt} [58]. The large scattering space might also give rise to significant multi-phonon electronic scattering rates [59]. Furthermore, AMSET has a quite approximate account of scattering rates. The accuracy of simple Thomas-Fermi-based free-carrier screening to such large carrier concentrations as the p-type N_{opt} can be questioned [60]. Lastly, the relaxation time approximation in its entirety has been found to deviate significantly from more precise iterative approaches to solving the Boltzmann transport equation [61, 62]. Nonetheless, our study represents an important addition to the investigation of electron scattering in materials with low-dimensional band structures [28–33]. This finding indicates there is great potential to

find new materials with record-breaking thermoelectric performance.

Concerns can be raised regarding the realizability of Na_2TiSb . Yeu *et al.* [36] found it to be stable at 700 K with *ab initio* molecular dynamics, but the material has yet to be synthesized to the best of the authors' knowledge. Materials containing alkali metals, like Na, generally require more care during synthesis due to high reactivity with oxygen and water, and tend to suffer from degradation in use as a TE material at high temperature due to ionic diffusion. In addition, the high doping needed to reach the p-type N_{opt} could be difficult to achieve without significantly altering other properties of the material. On the other hand, it has been argued that materials with a high N_{opt} are less vulnerable to small changes in N stemming from impurities in the precursors, thereby reducing cost [63]. Finally, the toxicity of Tl will necessitate a high level of care during synthesis, in use, and when disposing of the material at the end of its lifetime.

We have used the lattice thermal conductivity numbers from Yue [36] and use the same method for calculating electronic transport, but still achieved different transport properties. The difference can be explained by some methodological choices. In our work, the HSE06 band structure was used for transport calculations, not PBEsol like in the previous work, resulting in differences in the band structure and a larger band gap than that reported by Yue. Second, the materials properties used in AMSET also differ; we have, e.g. found a significantly lower ionic contribution to the dielectric constant. Combined with the inclusion of free-carrier screening, the POP scattering rates are greatly reduced in our work. Finally, in this work, we used AMSET version 0.5.0, which improves on the calculation of wavefunction overlaps for scattering across Brillouin zone boundaries, a change that is likely to increase scattering rates.

Despite the practical issues of realizing this material, we believe that Na_2TiSb merits further investigation due to its very attractive band structure, and one should intensify the hunt for similar less-toxic compounds. Further work should include assessing the dopability and possible dopants, followed by synthesis and experimental characterization. We believe the insights from this exotic band structure can serve to formulate advanced design principles for other materials. Critically, our study emphasizes how energy isosurfaces that are delocalized in \mathbf{k} -space tend to have reduced electron scattering. The chemical and electronic similarity to PbTe [34] could provide new insights into improving already well-established TE material, or aid the design of novel, superior materials.

V. CONCLUSION

In this article, we have calculated the electronic transport properties of Na_2TiSb with scattering rates from

AMSET. The valence band displays 1D-like features that result in a sharp increase in the DOS close to the band gap, while retaining a high mobility. Despite the high DOS, the electron scattering is modest due to low wavefunction overlaps, large scattering distances in k -space, and high free-carrier screening. Combined with an ultra-low κ_ℓ , this results in an exceptionally high predicted zT over a wide range of temperatures. The results underline the huge potential of low-dimensional features in electronic band structures for high TE performance.

VI. ACKNOWLEDGMENT

Ø.A.G., O.M.L., and K.B. are supported by the Research Council of Norway through the Allotherm project (Project No. 314778). Computational resources were provided by the Norwegian e-infrastructure for research and education, Sigma2, through grant No. nn9711k. We acknowledge insightful discussions with G.J. Snyder.

Appendix A: Lattice thermal conductivity

Table II lists the κ_ℓ used for calculations of zT . The numbers on the left are extracted from Ref. [36], while the temperatures in between (right side) are interpolated with cubic splines.

TABLE II. Lattice thermal conductivity values.

T [K]	κ_ℓ [Wm ⁻¹ K ⁻¹]	T [K]	κ_ℓ [Wm ⁻¹ K ⁻¹]
200	0.65	250	0.53
300	0.44	350	0.38
400	0.35	450	0.32
500	0.30	550	0.28
600	0.27	650	0.26
700	0.24		

Appendix B: n-type electron transport properties

The n-type electron transport properties of Na₂TlSb at temperatures 200–700 K are shown in Fig. 8. The highly dispersive conduction band, with a high relaxation time, gives a μ around an order of magnitude larger than that of the p-type. However, the lower DOS results in S more quickly approaching zero in the high-doping regime, thereby limiting the PF. We still predict an impressive zT ranging from 1.5 at 300 K to 3.0 at 700 K. Interestingly, at 700 K the difference in effective mass and mobility results in a large negative S at low carrier concentration. As a result, Na₂TlSb has an n-type zT of 0.85 at 700 K without doping.

-
- [1] L. E. Bell, Cooling, Heating, Generating Power, and Recovering Waste Heat with Thermoelectric Systems, *Science* **321**, 1457 (2008).
 - [2] G. J. Snyder and E. S. Toberer, Complex thermoelectric materials, *Nature Materials* **7**, 105 (2008).
 - [3] J. Schwab, M. Bernecker, S. Fischer, B. Seyed Sadjjadi, M. Kober, F. Rinderknecht, and T. Siefkes, Exergy Analysis of the Prevailing Residential Heating System and Derivation of Future CO₂-Reduction Potential, *Energies* **15**, 3502 (2022).
 - [4] C. B. Vining, An inconvenient truth about thermoelectrics, *Nature Materials* **8**, 83 (2009).
 - [5] A. J. Minnich, M. S. Dresselhaus, Z. F. Ren, and G. Chen, Bulk nanostructured thermoelectric materials: Current research and future prospects, *Energy & Environmental Science* **2**, 466 (2009).
 - [6] V. C. S. Theja, V. Karthikeyan, D. S. Assi, and V. A. L. Roy, Insights into the Classification of Nanoinclusions of Composites for Thermoelectric Applications, *ACS Applied Electronic Materials* **4**, 4781 (2022).
 - [7] C. P. Heinrich, T. W. Day, W. G. Zeier, G. J. Snyder, and W. Tremel, Effect of Isovalent Substitution on the Thermoelectric Properties of the Cu₂ ZnGeSe_{4-x} S_x Series of Solid Solutions, *Journal of the American Chemical Society* **136**, 442 (2014).
 - [8] S. N. H. Eliassen, A. Katre, G. K. H. Madsen, C. Persson, O. M. Løvrvik, and K. Berland, Lattice thermal conductivity of Ti_xZr_{1-x}Hf_{1-y}NiSn half-Heusler alloys calculated from first principles: Key role of nature of phonon modes, *Physical Review B* **95**, 045202 (2017).
 - [9] R. Tranås, O. M. Løvrvik, and K. Berland, Attaining Low Lattice Thermal Conductivity in Half-Heusler Sublattice Solid Solutions: Which Substitution Site Is Most Effective?, *Electronic Materials* **3**, 1 (2022).
 - [10] S. Wang, C. Chang, S. Bai, B. Qin, Y. Zhu, S. Zhan, J. Zheng, S. Tang, and L.-D. Zhao, Fine Tuning of Defects Enables High Carrier Mobility and Enhanced Thermoelectric Performance of n-Type PbTe, *Chemistry of Materials* **35**, 755 (2023).
 - [11] S. V. Faleev and F. Léonard, Theory of enhancement of thermoelectric properties of materials with nanoinclusions, *Physical Review B* **77**, 214304 (2008).
 - [12] C. Gayner and Y. Amouyal, Energy Filtering of Charge Carriers: Current Trends, Challenges, and Prospects for Thermoelectric Materials, *Advanced Functional Materials* **30**, 1901789 (2020).
 - [13] Y. Lin, M. Wood, K. Imasato, J. J. Kuo, D. Lam, A. N. Mortazavi, T. J. Slade, S. A. Hodge, K. Xi, M. G. Kanatzidis, D. R. Clarke, M. C. Hersam, and G. J. Snyder, Expression of interfacial Seebeck coefficient through grain boundary engineering with multi-layer graphene nanoplatelets, *Energy & Environmental Science* **13**, 4114 (2020).
 - [14] J. P. Heremans, V. Jovovic, E. S. Toberer, A. Samrat, K. Kurosaki, A. Charoenphakdee, S. Yamanaka, and G. J. Snyder, Enhancement of Thermoelectric Efficiency in PbTe by Distortion of the Electronic Density of States, *Science* **321**, 554 (2008).

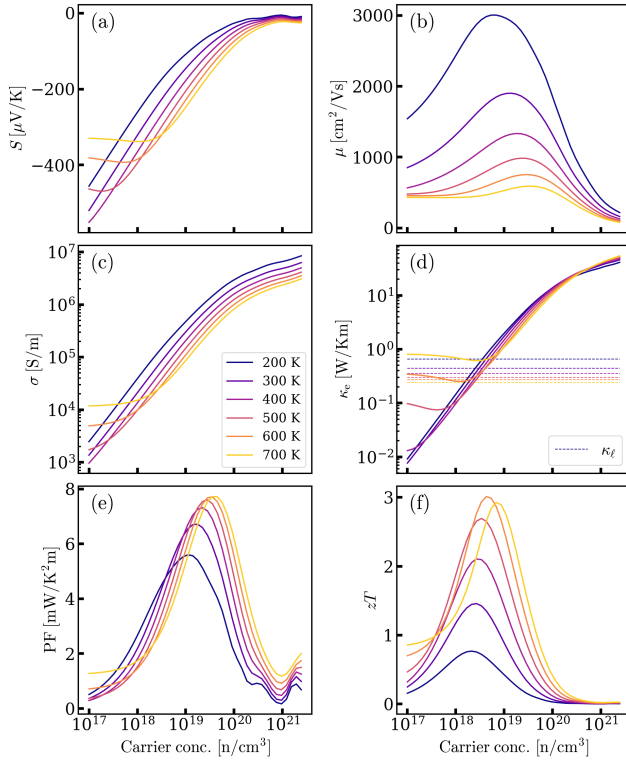


FIG. 8. The Seebeck coefficient, electrical conductivity, electron thermal conductivity, power factor, and figure of merit of n-type Na_2TlSb at temperatures 200–700 K.

- [15] J. Zhang, L. Song, G. K. H. Madsen, K. F. F. Fischer, W. Zhang, X. Shi, and B. B. Iversen, Designing high-performance layered thermoelectric materials through orbital engineering, *Nature Communications* **7**, 10892 (2016).
- [16] J. Li, S. Zhang, B. Wang, S. Liu, L. Yue, G. Lu, and S. Zheng, Designing high-performance n-type Mg_3Sb_2 -based thermoelectric materials through forming solid solutions and biaxial strain, *Journal of Materials Chemistry A* **6**, 20454 (2018).
- [17] Y. Pei, X. Shi, A. LaLonde, H. Wang, L. Chen, and G. J. Snyder, Convergence of electronic bands for high performance bulk thermoelectrics, *Nature* **473**, 66 (2011).
- [18] Y. Zhu, D. Wang, T. Hong, L. Hu, T. Ina, S. Zhan, B. Qin, H. Shi, L. Su, X. Gao, and L.-D. Zhao, Multiple valence bands convergence and strong phonon scattering lead to high thermoelectric performance in p-type PbSe , *Nature Communications* **13**, 4179 (2022).
- [19] D. Bilc, S. D. Mahanti, E. Quarez, K.-F. Hsu, R. Pcionek, and M. G. Kanatzidis, Resonant States in the Electronic Structure of the High Performance Thermoelectrics $\text{AgPb}_2\text{mSbTe}_{2+m}$: The Role of Ag-Sb Microstructures, *Physical Review Letters* **93**, 146403 (2004).
- [20] J. P. Heremans, B. Wiendlocha, and A. M. Chamoire, Resonant levels in bulk thermoelectric semiconductors, *Energy Environ. Sci.* **5**, 5510 (2012).
- [21] L. D. Hicks and M. S. Dresselhaus, Effect of quantum-well structures on the thermoelectric figure of merit, *Physical Review B* **47**, 12727 (1993).
- [22] L. D. Hicks and M. S. Dresselhaus, Thermoelectric figure of merit of a one-dimensional conductor, *Physical Review B* **47**, 16631 (1993).
- [23] A. I. Boukai, Y. Bunimovich, J. Tahir-Kheli, J.-K. Yu, W. A. Goddard III, and J. R. Heath, Silicon nanowires as efficient thermoelectric materials, *Nature* **451**, 168 (2008).
- [24] A. I. Hochbaum, R. Chen, R. D. Delgado, W. Liang, E. C. Garnett, M. Najarian, A. Majumdar, and P. Yang, Enhanced thermoelectric performance of rough silicon nanowires, *Nature* **451**, 163 (2008).
- [25] R. Venkatasubramanian, E. Siivola, T. Colpitts, and B. O'Quinn, Thin-film thermoelectric devices with high room-temperature figures of merit, *Nature* **413**, 597 (2001).
- [26] J. E. Cornett and O. Rabin, Thermoelectric figure of merit calculations for semiconducting nanowires, *Applied Physics Letters* **98**, 182104 (2011).
- [27] J. E. Cornett and O. Rabin, Universal scaling relations for the thermoelectric power factor of semiconducting nanostructures, *Physical Review B* **84**, 205410 (2011).
- [28] D. Parker, X. Chen, and D. J. Singh, High Three-Dimensional Thermoelectric Performance from Low-Dimensional Bands, *Physical Review Letters* **110**, 146601 (2013).
- [29] D. I. Bilc, G. Hautier, D. Waroquiers, G.-M. Rignanese, and P. Ghosez, Low-Dimensional Transport and Large Thermoelectric Power Factors in Bulk Semiconductors by Band Engineering of Highly Directional Electronic States, *Physical Review Letters* **114**, 136601 (2015).
- [30] M. T. Dylla, S. D. Kang, and G. J. Snyder, Effect of Two-Dimensional Crystal Orbitals on Fermi Surfaces and Electron Transport in Three-Dimensional Perovskite Oxides, *Angewandte Chemie International Edition* **58**, 5503 (2019).
- [31] J. Park, Y. Xia, V. Ozoliņš, and A. Jain, Optimal band structure for thermoelectrics with realistic scattering and bands, *npj Computational Materials* **7**, 43 (2021).
- [32] M. K. Brod and G. J. Snyder, Orbital chemistry of high valence band convergence and low-dimensional topology in PbTe , *Journal of Materials Chemistry A* **9**, 12119 (2021).
- [33] Ø. A. Grimenes, G. J. Snyder, O. M. Løvvik, and K. Berland, Thermoelectric transport of strained CsK_2Sb : Role of electron velocities and scattering within extended Fermi surfaces, *Physical Review B* **111**, 195205 (2025).
- [34] M. K. Brod, M. Y. Toriyama, and G. J. Snyder, Orbital Chemistry That Leads to High Valley Degeneracy in PbTe , *Chemistry of Materials* **32**, 9771 (2020).
- [35] J. He, Y. Xia, S. S. Naghavi, V. Ozoliņš, and C. Wolverton, Designing chemical analogs to PbTe with intrinsic high band degeneracy and low lattice thermal conductivity, *Nature Communications* **10**, 719 (2019).
- [36] T. Yue, Y. Zhao, J. Ni, S. Meng, and Z. Dai, Strong quartic anharmonicity, ultralow thermal conductivity, high band degeneracy and good thermoelectric performance in Na_2TlSb , *npj Computational Materials* **9**, 17 (2023).
- [37] R. Tranås, O. M. Løvvik, and K. Berland, Lattice Thermal Conductivity from First Principles and Active Learning with Gaussian Process Regression (2023).
- [38] J. M. Ziman, *Electrons and Phonons: The Theory of Transport Phenomena in Solids* (Clarendon Press, Oxford, 1960).

- [39] G. K. Madsen, J. Carrete, and M. J. Verstraete, BoltzTraP2, a program for interpolating band structures and calculating semi-classical transport coefficients, *Computer Physics Communications* **231**, 140 (2018).
- [40] A. M. Ganose, J. Park, A. Faghaninia, R. Woods-Robinson, K. A. Persson, and A. Jain, Efficient calculation of carrier scattering rates from first principles, *Nature Communications* **12**, 2222 (2021).
- [41] W. Li, Electrical transport limited by electron-phonon coupling from Boltzmann transport equation: An *ab initio* study of Si, Al, and MoS₂, *Physical Review B* **92**, 075405 (2015).
- [42] S. Ponc , W. Li, S. Reichardt, and F. Giustino, First-principles calculations of charge carrier mobility and conductivity in bulk semiconductors and two-dimensional materials, *Reports on Progress in Physics* **83**, 036501 (2020).
- [43] A. Matthiessen, Ueber die elektrische Leitungsf higkeit der Legirungen, *Annalen der Physik* **186**, 190 (1860).
- [44] G. Kresse and J. Hafner, *Ab Initio* molecular dynamics for liquid metals, *Physical Review B* **47**, 558 (1993).
- [45] G. Kresse and D. Joubert, From ultrasoft pseudopotentials to the projector augmented-wave method, *Physical Review B* **59**, 1758 (1999).
- [46] K. Berland and P. Hyldgaard, Exchange functional that tests the robustness of the plasmon description of the van der Waals density functional, *Physical Review B* **89**, 035412 (2014).
- [47] K. Berland, C. A. Arter, V. R. Cooper, K. Lee, B. I. Lundqvist, E. Schr der, T. Thonhauser, and P. Hyldgaard, Van der Waals density functionals built upon the electron-gas tradition: Facing the challenge of competing interactions, *The Journal of Chemical Physics* **140**, 18A539 (2014).
- [48] K. Berland, V. R. Cooper, K. Lee, E. Schr der, T. Thonhauser, P. Hyldgaard, and B. I. Lundqvist, Van der Waals forces in density functional theory: A review of the vdW-DF method, *Reports on Progress in Physics* **78**, 066501 (2015).
- [49] Y. Le Page and P. Saxe, Symmetry-general least-squares extraction of elastic data for strained materials from *ab initio* calculations of stress, *Physical Review B* **65**, 104104 (2002).
- [50] M. Gajdo , K. Hummer, G. Kresse, J. Furthm ller, and F. Bechstedt, Linear optical properties in the projector-augmented wave methodology, *Physical Review B* **73**, 045112 (2006).
- [51] A. V. Krukau, O. A. Vydrov, A. F. Izmaylov, and G. E. Scuseria, Influence of the exchange screening parameter on the performance of screened hybrid functionals, *The Journal of Chemical Physics* **125**, 224106 (2006).
- [52] A. Jain, S. P. Ong, G. Hautier, W. Chen, W. D. Richards, S. Dacek, S. Cholia, D. Gunter, D. Skinner, G. Ceder, and K. A. Persson, Commentary: The Materials Project: A materials genome approach to accelerating materials innovation, *APL Materials* **1**, 011002 (2013).
- [53] J. P. Perdew, A. Ruzsinszky, G. I. Csonka, O. A. Vydrov, G. E. Scuseria, L. A. Constantin, X. Zhou, and K. Burke, Restoring the Density-Gradient Expansion for Exchange in Solids and Surfaces, *Physical Review Letters* **100**, 136406 (2008).
- [54] E. Isotta, W. Peng, A. Balodhi, and A. Zevkink, Elastic Moduli: A Tool for Understanding Chemical Bonding and Thermal Transport in Thermoelectric Materials, *Angewandte Chemie* **135**, e202213649 (2023).
- [55] A. Ganose, A. Searle, A. Jain, and S. Griffin, IFermi: A python library for Fermi surface generation and analysis, *Journal of Open Source Software* **6**, 3089 (2021).
- [56] See Supplemental Material at [URL will be inserted by publisher] free-carrier screening at 600 K, deformation potentials, and zT calculated without free-carrier screening.
- [57] J. Park, M. Dylla, Y. Xia, M. Wood, G. J. Snyder, and A. Jain, When band convergence is not beneficial for thermoelectrics, *Nature Communications* **12**, 3425 (2021).
- [58] M. V. Fischetti, Effect of the electron-plasmon interaction on the electron mobility in silicon, *Physical Review B* **44**, 5527 (1991).
- [59] N.-E. Lee, J.-J. Zhou, H.-Y. Chen, and M. Bernardi, *Ab initio* electron-two-phonon scattering in GaAs from next-to-leading order perturbation theory, *Nature Communications* **11**, 1607 (2020).
- [60] Y. Go, R. Dutt, and N. Neophytou, Theory of quasistatically screened electron-polar optical phonon scattering, *Physical Review B* **111**, 195211 (2025).
- [61] R. Claes, G. Brunin, M. Giantomassi, G.-M. Rignanese, and G. Hautier, Assessing the quality of relaxation-time approximations with fully automated computations of phonon-limited mobilities, *Physical Review B* **106**, 094302 (2022).
- [62] R. Claes, S. Ponc , G.-M. Rignanese, and G. Hautier, Phonon-limited electronic transport through first principles, *Nature Reviews Physics* **7**, 73 (2025).
- [63] Q. Lou, Z. Gao, S. Han, F. Liu, C. Fu, and T. Zhu, High Defect Tolerance in Heavy-Band Thermoelectrics, *Advanced Energy Materials* , 2402399 (2024).

Exceptional thermoelectric properties in Na_2TlSb enabled by quasi-1D band structure

Øven A. Grimenes,¹ Ole M. Løvvik,² and Kristian Berland¹

¹*Department of Mechanical Engineering and Technology Management,
Norwegian University of Life Sciences, NO-1432 Ås, Norway*

²*SINTEF Sustainable Energy Technology,
Forskningsveien 1, NO-0314 Oslo, Norway*

(Dated: June 30, 2025)

S1. FREE-CARRIER SCREENING

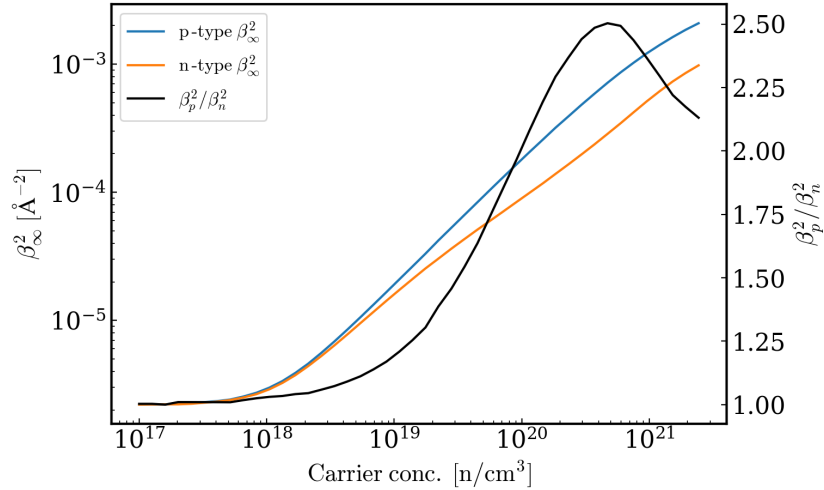


FIG. S1. Inversehigh-frequency free-carrier screening length for p- and n-type Na_2TlSb at 600 K for various carrier concentrations and the ratio between them.

S2. DEFORMATION POTENTIALS

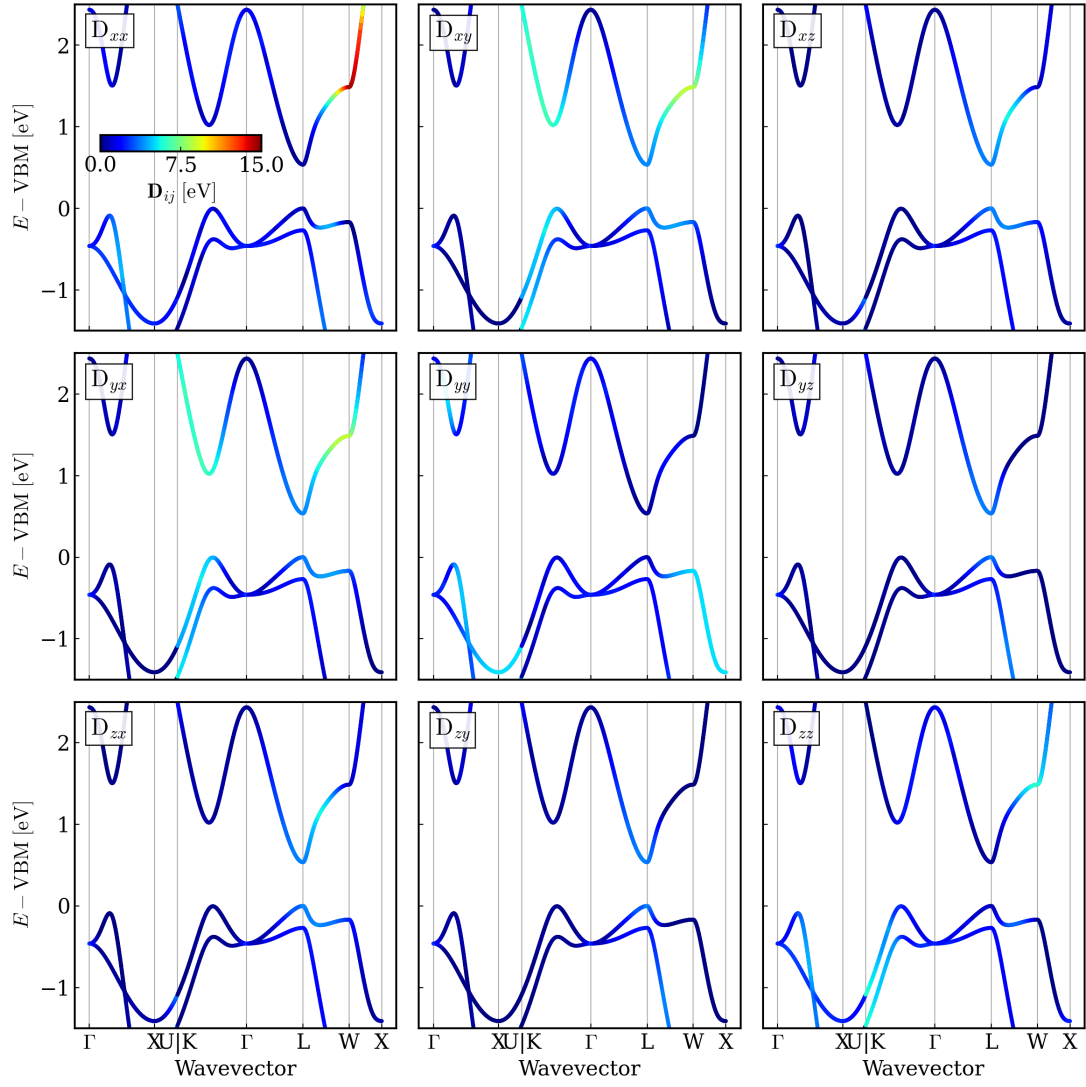


FIG. S2. Tensor components of the deformation potential of Na_2TiSb projected onto the band structure.

S3. zT WITHOUT FREE-CARRIER SCREENING

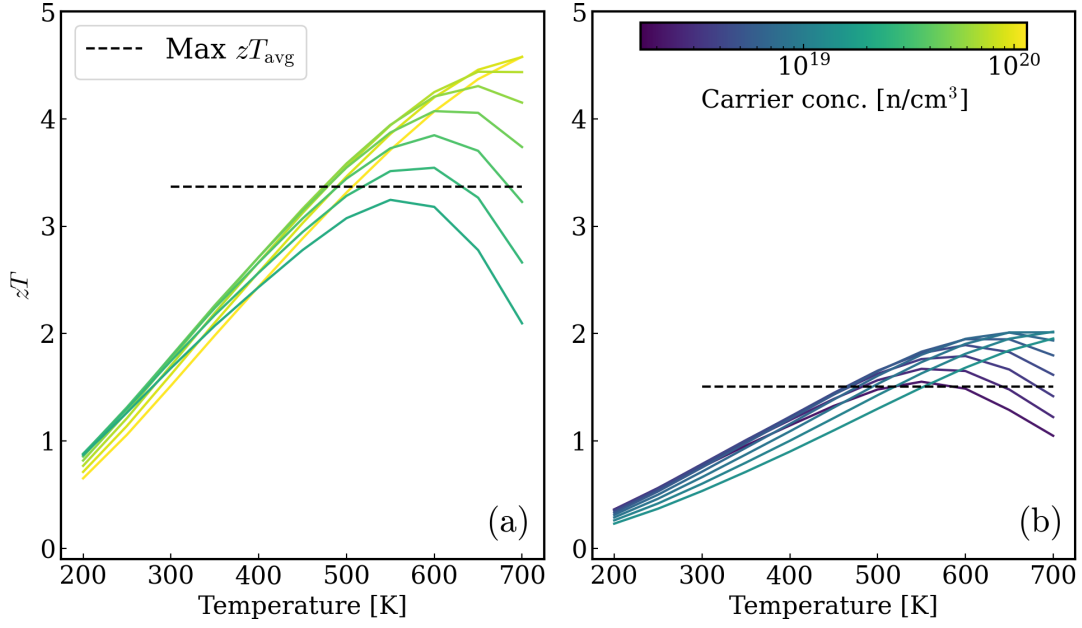


FIG. S3. p- and n-type zT of $N_{22}TlSb$ as a function of temperature when free-carrier screening is not included. the zT_{avg} of p-type is almost as high as with free-carrier screening included due to reduced bipolar transport at high temperatures.